Available online at www.sciencedirect.com
ScienceDirect
International Journal of Heat and Mass Transfer 50 (2007) 734–745
International Journal of HEAT and MASS TRANSFER
www.elsevier.com/locate/ijhmt

Modeling study on the characteristics of laminar and turbulent argon plasma jets impinging normally upon a flat plate in ambient air

Hai-Xing Wang [a], Xi Chen [b,*], Kai Cheng [b], Wenxia Pan [c]

[a] School of Astronautics, Beijing University of Aeronautics and Astronautics, Beijing 100083, China
[b] Department of Engineering Mechanics, Tsinghua University, Beijing 100084, China
[c] Institute of Mechanics, Chinese Academy of Sciences, Beijing 100080, China

Received 16 February 2006; received in revised form 5 July 2006
Available online 8 September 2006

Abstract

Modeling study is performed to compare the flow and heat transfer characteristics of laminar and turbulent argon thermal-plasma jets impinging normally upon a flat plate in ambient air. The combined-diffusion-coefficient method and the turbulence-enhanced combined-diffusion-coefficient method are employed to treat the diffusion of argon in the argon–air mixture for the laminar and the turbulent cases, respectively. Modeling results presented include the flow, temperature and argon concentration fields, the air mass flow-rates entrained into the impinging plasma jets, and the distributions of the heat flux density on the plate surface. It is found that the formation of a radial wall jet on the plate surface appreciably enhances the mass flow rate of the ambient air entrained into the laminar or turbulent plasma impinging-jet. When the plate standoff distance is comparatively small, there exists a significant difference between the laminar and turbulent plasma impinging-jets in their flow fields due to the occurrence of a large closed recirculation vortex in the turbulent plasma impinging-jet, and no appreciable difference is found between the two types of jets in their maximum values and distributions of the heat flux density at the plate surface. At larger plate standoff distances, the effect of the plate on the jet flow fields only appears in the region near the plate, and the axial decaying-rates of the plasma temperature, axial velocity and argon mass fraction along the axis of the laminar plasma impinging-jet become appreciably less than their turbulent counterparts.

Keywords: Thermal plasma; Laminar and turbulent impinging-jets; Air entrainment; Modeling

1. Introduction

Thermal plasma jets impinging upon substrates or workpieces are encountered in many applications of thermal plasmas in materials processing, such as plasma spraying, plasma cladding or re-melting hardening of materials surfaces, plasma preparation of functional films, etc. [1,2]. With the plasma spraying as the main research background, numerous experimental and modeling studies have been performed in past decades concerning the plasma jet characteristics without or with accounting for the presence of a substrate (e.g. see [1–16] and the references cited therein). In most of the practical applications, the working-gas flow rate of the DC arc plasma torch for generating the thermal plasma jet is comparatively large and the arc root locations at the anode surface and the arc itself in the torch nozzle are often in unceasing motion, and thus the thermal plasma jet ejected from the plasma torch is usually in a turbulent flow state. The turbulent plasma jets are always accompanied by large flow fluctuations, intensive noise emission, strong entrainment of surrounding gas into the plasma jets and thus with short lengths of the high-temperature region and steep axial gradients of plasma parameters (temperature, axial velocity, etc.). These special features of the turbulent plasma jets are often not favorable from the viewpoint of materials processing, because they will worsen the working surroundings of operators, reduce

* Corresponding author. Tel.: +86 10 62784127; fax: +86 10 62781824.
E-mail address: cx-dem@mail.tsinghua.edu.cn (X. Chen).

0017-9310/$ - see front matter © 2006 Elsevier Ltd. All rights reserved.
doi:10.1016/j.ijheatmasstransfer.2006.07.002

Nomenclature

c_p	specific heat at constant pressure (J kg^{-1} K^{-1})
$\overline{D}^{x}_{AB}$	combined ordinary diffusion coefficient (m^2 s^{-1})
$\overline{D}^{T}_{AB}$	combined thermal diffusion coefficient (kg m^{-1} s^{-1})
F_e	net axial mass flux of the entrained air (kg s^{-1})
f_A	argon mass fraction in argon–air mixture
G	turbulence generation term (kg m^{-1} s^{-3})
h	specific enthalpy (J kg^{-1})
J	diffusion mass flux vector (kg m^{-2} s^{-1})
k	thermal conductivity (W m^{-1} K^{-1})
K	turbulent kinetic energy (m^2 s^{-2})
L	plate standoff distance (m)
$\bar{m}$	average mass of all the heavy particles (excluding electrons) (kg)
$\overline{M}$	average mass of all the gas particles (including electrons) (kg)
n	gas-particle number density (m^{-3})
p	pressure (Pa)
Pr	Prandtl number
q	heat flux density (W m^{-2})
R	outer radius of computational domain (m)
R_{in}	plasma jet inlet (or torch exit) radius (m)
r, x	radial and axial coordinates (m)
Sc	Schmidt number
S_f	source term in species diffusion equation (kg m^{-3} s^{-1})
T	temperature (K)
T_0	highest temperature at jet-inlet center (K)
u, v	axial and radial velocity components (m s^{-1})
U_0	maximum axial velocity at jet-inlet center (m s^{-1})
U_r	radiation power per unit volume of plasma (W m^{-3})
X_A	argon mole fraction

Greek symbols

ε	turbulence dissipation rate (m^2 s^{-3})
Γ_f	transport coefficient in species conservation equation (kg m^{-1} s^{-1})
μ	viscosity (Pa s)
ρ	mass density (kg m^{-3})

Subscripts

0	jet-inlet center
A	gas A (argon)
B	gas B (air)
f	for mass fraction
K	for turbulence kinetic energy
L	for laminar
T	for turbulent
ε	for turbulent dissipation rate

the process repeatability and controllability, and increase the oxidization degree of metallic materials processed in air surroundings.

Stable and silent long laminar plasma jets have been successfully generated at the atmospheric pressure in recent years with elaborately designed DC arc plasma torches [17–22]. Typical working parameters of the plasma torch for generating laminar plasma jets are as follows [20–22]: arc currents 75–220 A, argon mass flow rates $(1.6-3.7)\times10^{-4}$ kg s^{-1}, torch powers 4–11 kW; and the maximum temperature and axial velocity at the torch exit may vary in the ranges of 13,000–17,000 K and 600–1200 m s^{-1}. Since only molecular diffusion mechanism is involved in the laminar plasma jet, the entrainment of ambient air into the laminar plasma jet is significantly reduced. Consequently, the length of the high-temperature region in the laminar plasma jet is much longer than that in the conventional turbulent plasma jet. The axial gradients of plasma temperature, axial velocity and species concentration in the laminar plasma jet are also appreciably reduced. Moreover, the length of the laminar plasma jet can be adjusted easily by changing the arc current and/or the working-gas flow rate of the plasma torch used for generating the laminar plasma jet [20–22]. These merits of the long laminar plasma jet provide a new possibility to achieve low-noise working surroundings, better process repeatability and controllability, and reduced oxidation degree of metallic materials processed in air surroundings. Preliminary attempts [20,21,23–25] to use the laminar plasma jet in the preparation of thermal barrier coatings, in the re-melting hardening of cast iron and other metals and in the cladding hardening of stainless-steel surface have shown encouraging results such as the fine microstructure, low surface roughness and small porosity of the prepared coatings, the good re-melting process controllability and surface morphologies, as well as the preferable metallurgically bonded clad layer.

With the same DC non-transferred arc plasma torch, both laminar and turbulent thermal plasma jets can be generated in experiments [20–22] and thus it is possible to compare the characteristics of laminar and turbulent thermal plasma jets for a given plasma torch. Experimental observations [20,22] show that for a fixed arc current, silent long laminar plasma jets and noisy short turbulent plasma jets are generated, respectively, at lower and higher flow rates. Between the laminar and turbulent flow regimes there exists an unsteady transitional flow regime. The transitional plasma jet is not too useful for materials processing due to its unsteadiness, and thus we are mainly interested in the laminar and turbulent plasma jet characteristics. For the laminar plasma jet, the high-temperature region length increases notably with increasing working-gas flow rate or

arc current. On the other hand, the high-temperature region length for the turbulent plasma jet is much shorter and less dependent on the working-gas flow rate or arc current of the plasma torch.

In order to deepen our understanding of the laminar plasma jet and promote its applications, Ref. [26] performed a modeling study to compare the flow and heat transfer characteristics of laminar and turbulent argon plasma jets issuing freely into the ambient air. It was shown that the significant difference between the characteristics of the laminar and turbulent plasma jets is due to that different transport mechanisms (molecular mechanism is associated with the laminar jets, while turbulent mechanism is dominant in the turbulent jets) and thus quite different air-entrainment laws are involved in the two types of plasma jets.

With the plasma re-melting and cladding hardening of materials surfaces as the main research background [20,21,23–25,27], this paper, as a continuation of [26], performs a modeling study to compare the flow and heat transfer characteristics of the laminar and turbulent argon plasma jets impinging normally upon a flat plate in the ambient air. To our knowledge, so far no such a comparative study has been conducted, although many papers were published concerning the fluid flow and heat/mass transfer characteristics of isothermal gas and flame jets impinging upon a flat plate (e.g. see the review papers [28–30]). In this study, the combined-diffusion-coefficient method proposed by Murphy [31,32] is employed to treat the diffusion of the ambient air into the laminar argon plasma jet, while the turbulence-enhanced combined-diffusion-coefficient method [15] is used to deal with the entrainment of the ambient air into the turbulent argon plasma jet, similarly to [26].

2. Modeling approach

The main assumptions employed in this study include (i) the jet flow is steady and axi-symmetrical; (ii) the plasma is in the local thermodynamic equilibrium (LTE) state and optically thin to radiation; (iii) the swirling velocity component can be neglected in comparison with the axial velocity; (iv) the diffusion of argon within the argon–air mixture can be handled by the combined-diffusion-coefficient method [31–33] for the laminar case and by the turbulence-enhanced combined-diffusion-coefficient method [15] for the turbulent case; and (v) the buoyancy effects can be ignored due to their smallness [33,34].

The continuity, momentum and energy equations for the *laminar* plasma jet case can thus be written as follows [26,33]:

$$\frac{\partial}{\partial x}(\rho u)+\frac{1}{r}\frac{\partial}{\partial r}(r\rho v)=0 \tag{1}$$

$$\frac{\partial(\rho uu)}{\partial x}+\frac{1}{r}\frac{\partial(r\rho uv)}{\partial r} =-\frac{\partial p}{\partial x}+2\frac{\partial}{\partial x}\left(\mu\frac{\partial u}{\partial x}\right)+\frac{1}{r}\frac{\partial}{\partial r}\left[r\mu\left(\frac{\partial u}{\partial r}+\frac{\partial v}{\partial x}\right)\right] \tag{2}$$

$$\frac{\partial(\rho uv)}{\partial x}+\frac{1}{r}\frac{\partial(r\rho vv)}{\partial r} =-\frac{\partial p}{\partial r}+\frac{2}{r}\frac{\partial}{\partial r}\left(r\mu\frac{\partial v}{\partial r}\right)+\frac{\partial}{\partial x}\left[\mu\left(\frac{\partial v}{\partial x}+\frac{\partial u}{\partial r}\right)\right]-2\mu\frac{v}{r^2} \tag{3}$$

$$\frac{\partial(\rho uh)}{\partial x}+\frac{1}{r}\frac{\partial(r\rho vh)}{\partial r} =\frac{\partial}{\partial x}\left[\frac{k}{c_p}\frac{\partial h}{\partial x}\right]+\frac{1}{r}\frac{\partial}{\partial r}\left[r\frac{k}{c_p}\frac{\partial h}{\partial r}\right]-U_r-\frac{\partial}{\partial x}[(h_A-h_B)J_x] -\frac{1}{r}\frac{\partial}{\partial r}[r(h_A-h_B)J_r]-\frac{\partial}{\partial x}\left[\frac{k}{c_p}(h_A-h_B)\frac{\partial f_A}{\partial x}\right] -\frac{1}{r}\frac{\partial}{\partial r}\left[r\frac{k}{c_p}(h_A-h_B)\frac{\partial f_A}{\partial r}\right] \tag{4}$$

Here u and v are the axial (x-) and radial (r-) velocity components; p the pressure; and ρ, μ, k, c_p, h and U_r are the temperature- and composition-dependent plasma density, viscosity, thermal conductivity, specific heat at constant pressure, specific enthalpy and radiation power per unit volume of plasma, respectively. In Eq. (4), the terms containing (h_A-h_B) represent the contribution of species diffusion to the energy transport, where h_A and h_B are the temperature-dependent specific enthalpies of gases A (pure argon) and B (pure air), respectively. f_A is the mass fraction of argon in the argon–air mixture and is solved by use of the following species conservation equation [26,33]:

$$\frac{\partial(\rho uf_A)}{\partial x}+\frac{1}{r}\frac{\partial(r\rho vf_A)}{\partial r}=\frac{\partial}{\partial x}\left[\Gamma_f\frac{\partial f_A}{\partial x}\right]+\frac{1}{r}\frac{\partial}{\partial r}\left[r\Gamma_f\frac{\partial f_A}{\partial r}\right]+S_f \tag{5}$$

J_x and J_r are the axial (x-) and radial (r-) components of the following argon diffusion mass flux vector [31]:

$$\mathbf{J}_A=-(n^2/\rho)\bar{m}_A\bar{m}_B\overline{D}^x_{AB}\nabla X_A-\overline{D}^T_{AB}\nabla\ln T \tag{6}$$

where n is the total gas-particle number density, $\bar{m}_A$ and $\bar{m}_B$ are the averaged gas-particle masses for all the heavy particles (excluding electrons) coming from argon and those from air, X_A is the mole fraction of argon in the mixture, whereas $\overline{D}^x_{AB}$ and $\overline{D}^T_{AB}$ are the combined ordinary diffusion coefficient associated with the argon mole-fraction gradient ∇X_A and the combined thermal diffusion coefficient associated with the temperature gradient ∇T, respectively [31]. The transport coefficient in Eq. (5) can be expressed as [26,33] $\Gamma_f=[\bar{m}_A\bar{m}_B/(\overline{M}\overline{M}_A)]\rho\overline{D}^x_{AB}$, in which $\overline{M}$ and $\overline{M}_A$ are the averaged gas-particle mass for all the gas particles (including electrons) of the gas mixture and that for all the gas particles coming from argon [31], respectively. The source term S_f in Eq. (5) is expressed as [26,33]

$$S_f=\frac{1}{r}\frac{\partial}{\partial r}\left(r\Gamma_f\frac{f_A}{\overline{M}}\frac{\partial\overline{M}}{\partial r}\right)-\frac{1}{r}\frac{\partial}{\partial r}\left(r\Gamma_f\frac{f_A}{\overline{M}_A}\frac{\partial\overline{M}_A}{\partial r}\right) +\frac{\partial}{\partial x}\left(\Gamma_f\frac{f_A}{\overline{M}}\frac{\partial\overline{M}}{\partial x}\right)-\frac{\partial}{\partial x}\left(\Gamma_f\frac{f_A}{\overline{M}_A}\frac{\partial\overline{M}_A}{\partial x}\right) +\frac{1}{r}\frac{\partial}{\partial r}\left(r\overline{D}^T_{AB}\frac{\partial\ln T}{\partial r}\right)+\frac{\partial}{\partial x}\left(\overline{D}^T_{AB}\frac{\partial\ln T}{\partial x}\right) \tag{7}$$

On the other hand, for the study of the characteristics of *turbulent* argon plasma jets issuing into the ambient air, Eqs. (1)–(7) are still be employed but all the physical quantities appearing in those equations are their time-averaged values. In addition, the molecular transport coefficients appearing in the conservation equations (2)–(5) are substituted by their counterparts containing both the turbulent and molecular contributions. Namely, μ in Eqs. (2) and (3) is substituted by $(\mu_T + \mu)$, k/c_p in Eq. (4) substituted by $\lfloor(\mu_T/Pr_h) + (k/c_p)\rfloor$, and Γ_f in Eq. (5) is substituted by $\lfloor(\mu_T/Sc_f) + \Gamma_f\rfloor$. In addition, an additional term representing the turbulent diffusion flux, i.e. $-(\mu_T/Sc_f)\nabla f_A$, is added into the right-hand side of Eq. (6) for the argon diffusion mass flux vector $\mathbf{J}_A$. Here μ_T is the turbulent viscosity, and μ_T is calculated by $\mu_T = C_\mu \rho K^2/\varepsilon$ when the K–ε two-equation turbulence model is employed. K and ε are the turbulent kinetic energy and its dissipation rate, and are solved by

$$\frac{\partial(\rho u K)}{\partial x} + \frac{1}{r}\frac{\partial(rv\rho K)}{\partial r} = \frac{\partial}{\partial x}\left[\left(\mu + \frac{\mu_T}{Pr_K}\right)\frac{\partial K}{\partial x}\right] + \frac{1}{r}\frac{\partial}{\partial r}\left[r\left(\mu + \frac{\mu_T}{Pr_K}\right)\frac{\partial K}{\partial r}\right] + G - \rho\varepsilon \tag{8}$$

$$\frac{\partial(\rho u \varepsilon)}{\partial x} + \frac{1}{r}\frac{\partial(rv\rho\varepsilon)}{\partial r} = \frac{\partial}{\partial x}\left[\left(\mu + \frac{\mu_T}{Pr_\varepsilon}\right)\frac{\partial \varepsilon}{\partial x}\right] + \frac{1}{r}\frac{\partial}{\partial r}\left[r\left(\mu + \frac{\mu_T}{Pr_\varepsilon}\right)\frac{\partial \varepsilon}{\partial r}\right] + \frac{\varepsilon}{K}(C_1 G - C_2\rho\varepsilon) \tag{9}$$

C_μ, C_1, C_2, Pr_h, Sc_f, Pr_K and Pr_ε are constants in the turbulence model, and in this study they are taken to be their commonly adopted values, i.e. 0.09, 1.44, 1.92, 0.9, 1.0, 1.0 and 1.3, respectively. The turbulence generation term, G, in Eqs. (8) and (9) is expressed as

$$G = \mu_T\left[2\left(\frac{\partial u}{\partial x}\right)^2 + 2\left(\frac{\partial v}{\partial r}\right)^2 + 2\left(\frac{v}{r}\right)^2 + \left(\frac{\partial u}{\partial r} + \frac{\partial v}{\partial x}\right)^2\right] \tag{10}$$

The computational domain used in the modeling is denoted as A–B–C–D–E–A in Fig. 1. The radius of the jet inlet (A–B) is 4 mm. D–E is the flat plate impinged by the plasma jet, and the radial size (DE or AC) of the computational domain is taken to be 50 mm. The axial size (CD or AE) can vary in the range of 10–100 mm to investigate the effect of the distance between the flat plate and the torch exit or jet inlet (will be denoted by L and called the plate standoff distance hereafter). Boundary conditions are as follows.

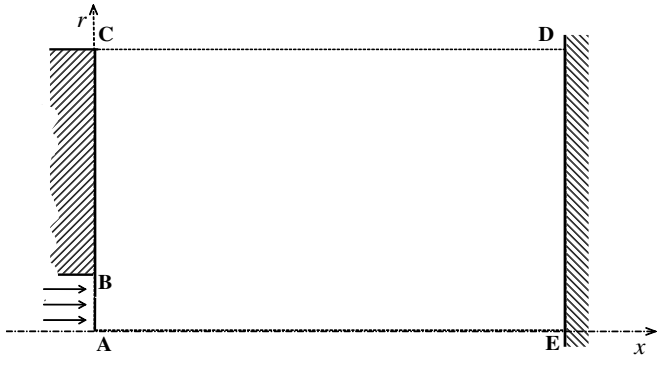

Fig. 1. Computational domain used for the plasma impinging-jet modeling.

(i) At the jet inlet (A–B): $v = 0$, $f_A = 1.0$, and the following profiles of axial velocity and temperature are used:

$$u = U_0[1 - (r/R_{in})^{1.4}],$$
$$T = (T_0 - T_w)[1 - (r/R_{in})^{2.3}] + T_w \tag{11}$$

in which R_{in} is the radius of the jet-inlet section (4 mm), T_w is the inner wall temperature of plasma torch and $T_w = 700$ K, whereas U_0 and T_0 are the maximum axial velocity and temperature at jet-inlet axis (U_0 will be called the jet-inlet velocity and T_0 the jet-inlet temperature hereafter), respectively. For the turbulent cases, $K = 0.00005 \times u^2$ and $\varepsilon = K^{3/2}/L_T$ are used at the jet-inlet section A–B, where $L_T = 0.075\delta_{0.1}/C_\mu^{3/4}$ and $\delta_{0.1}$ is the jet width defined by the radial distance at which the axial velocity reduces to $u = 0.1 \times U_0$ [14,15]. The axial velocity and temperature profiles (11) were employed in a few previous studies [14,15] and were shown to be able to predict plasma temperature, velocity and species concentration fields in reasonable agreement with correspondent experimental data for a typical turbulent argon plasma jet issuing into the ambient air. For facilitating the comparison of laminar and turbulent plasma impinging-jet characteristics, the same inlet velocity and temperature profiles are used in this study for both the laminar and turbulent plasma jets.

(ii) At the rear surface B–C of the plasma torch wall, for the laminar case, $u = v = 0$ and zero diffusion flux are employed, and the wall temperature is assumed to vary in the radial direction according to the relation $T = 700 - 400\frac{\ln(r/R_{in})}{\ln(R/R_{in})}$, in which R_{in} and R are the inner radius and outer radius of the plasma torch wall. For the turbulent jet case, wall function method is used to treat the B–C boundary conditions.

(iii) Along the outer free boundary C–D, the following conditions are employed:

$$\partial u/\partial r = 0, \quad \partial(\rho r v)/\partial r = 0,$$

and

$$\begin{aligned} &\text{if } v < 0: \quad T = 300 \text{ K}, \quad f_A = 0, \quad K = 0, \quad \varepsilon = 0 \\ &\text{if } v > 0: \quad \partial T/\partial r = 0, \quad \partial f_A/\partial r = 0, \\ &\qquad\qquad \partial K/\partial r = 0, \quad \partial\varepsilon/\partial r = 0 \end{aligned} \tag{12}$$

(iv) At the plate surface D–E, for the laminar case, $u = v = 0$ and zero diffusion flux are employed and the wall temperature is assumed to be 1000 K. For

the turbulent jet case, the wall function method is also used to treat the D–E boundary conditions.

(v) Along the jet axis A–E, the axi-symmetrical conditions are employed:

$$\partial\phi/\partial r = 0 \ \ (\phi = u, h, f_A, K, \varepsilon), \quad v = 0 \tag{13}$$

The SIMPLER algorithm [35] is used to solve the governing equations (1)–(5), (8) and (9) associated with their boundary conditions to obtain the velocity, specific enthalpy, argon mass fraction and turbulent parameter (for turbulent case) fields in the plasma jets. The temperature field can be easily calculated from the computed distributions of the specific enthalpy and argon mass fraction using the argon–air plasma property tables compiled for different temperatures and different argon mass fractions [32]. The number of grid points employed in the computation are 124 (x-) × 78 (r-direction). Non-uniform mesh is adopted with finer mesh spacing near the plate surface, the jet axis and the jet inlet. A numerical test shows that mesh-independent results have been obtained using the 124 × 78 mesh.

3. Modeling results and discussion

Typical modeling results are presented in Figs. 2–12 to compare the flow and heat/mass transfer characteristics of laminar and turbulent argon plasma jets impinging normally upon a flat plate in ambient air. In order to reveal more clearly the difference between the characteristics of laminar and turbulent plasma impinging-jets, the same values of the U_0 and T_0 in the radial profiles (11) will be used at first for both the laminar and turbulent cases. It is noted that in experiments almost the same U_0 and T_0 values may be obtained for both the laminar and turbulent plasma jets using some combinations of torch parameters [21,22].

For the practical applications of plasma jets in re-melting or cladding hardening of metallic materials surfaces [20,21,23–25,27], usually the plate standoff distance L is comparatively small, e.g. about 10 mm. Hence, our modeling studies are first concerned with such a case of smaller plate standoff distance, and after that the effects of the plate standoff distance on the impinging plasma jet characteristics will be investigated. For the case with the jet-inlet velocity $U_0 = 1000\ \mathrm{m\ s^{-1}}$ and temperature $T_0 = 14{,}000$ K

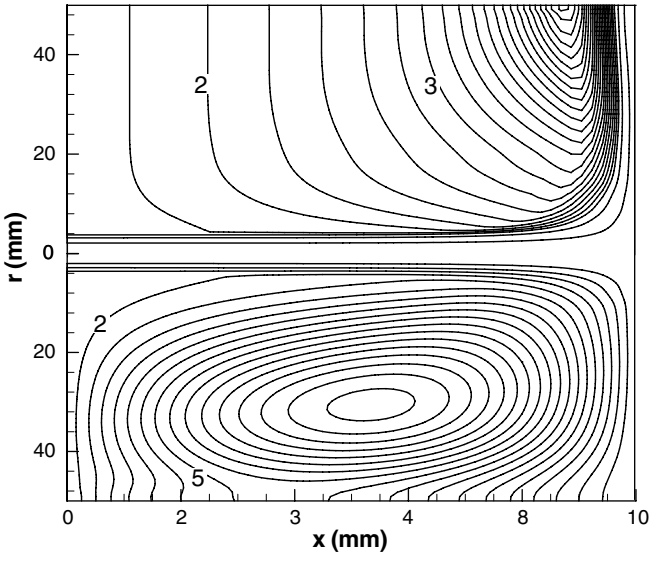

Fig. 2. Comparison of the computed streamlines in impinging plasma jets for the case with plate standoff distance $L = 10$ mm, jet-inlet velocity $U_0 = 1000\ \mathrm{m\ s^{-1}}$ and jet-inlet temperature $T_0 = 14{,}000$ K. The stream function is presented in $10^{-4}\ \mathrm{kg\ s^{-1}}$ per radian. Upper semi-plane – laminar jet, interval is $0.2 \times 10^{-4}\ \mathrm{kg\ s^{-1}}$ per radian; lower semi-plane – turbulent jet, interval is $0.5 \times 10^{-4}\ \mathrm{kg\ s^{-1}}$ per radian.

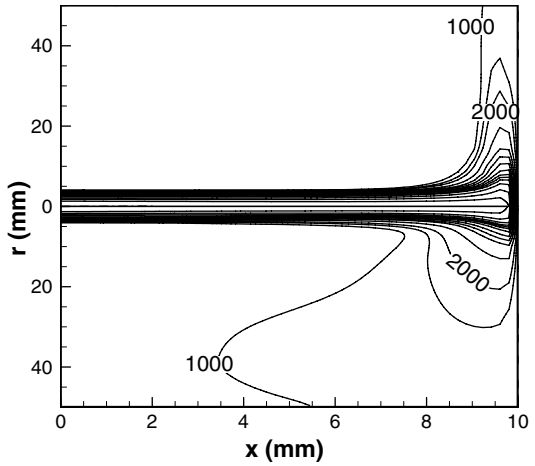

Fig. 3. Comparison of the isotherms in the impinging plasma jets for the case with $L = 10$ mm, $U_0 = 1000\ \mathrm{m\ s^{-1}}$ and $T_0 = 14{,}000$ K. Upper semi-plane – laminar jet; lower semi-plane – turbulent jet. Outermost isotherm is 1000 K; isotherm interval is 500 K for the outer three isotherms and 1000 K for others.

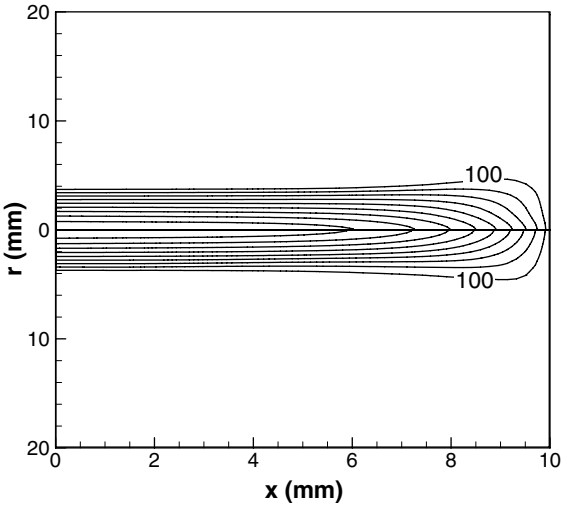

Fig. 4. Comparison of the axial velocity contours in the impinging plasma jets for the case with $L = 10$ mm, $U_0 = 1000\ \mathrm{m\ s^{-1}}$ and $T_0 = 14{,}000$ K. Upper semi-plane – laminar jet; lower semi-plane – turbulent jet. Outermost isoline is $100\ \mathrm{m\ s^{-1}}$ and interval is $100\ \mathrm{m\ s^{-1}}$.

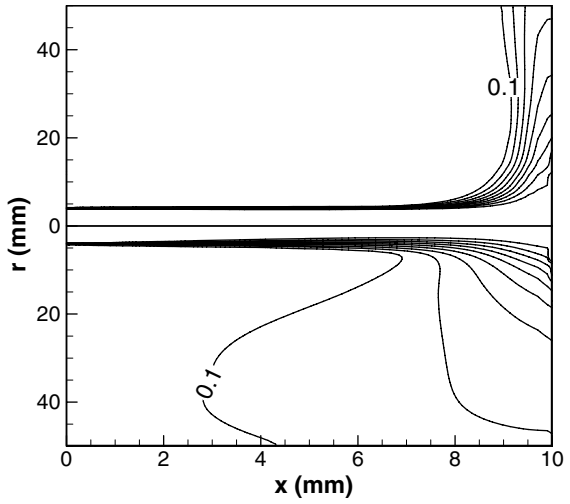

Fig. 5. Comparison of the argon mass fraction contours in impinging plasma jets for the case with $L = 10$ mm, $U_0 = 1000$ m s^{-1} and $T_0 = 14{,}000$ K. Upper semi-plane – laminar jet, lower semi-plane – turbulent jet. Outermost isoline is 0.1 and interval is 0.1.

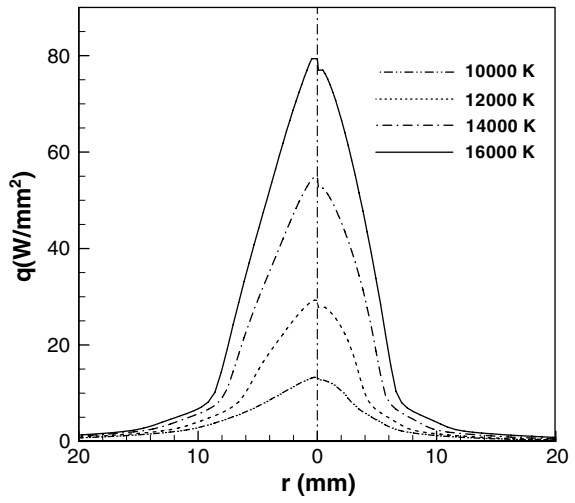

Fig. 6. Heat flux density distributions on the plate surface for the cases with a fixed jet-inlet velocity ($U_0 = 1000$ m s^{-1}) but different jet-inlet temperatures ($T_0 = 10{,}000$ K, 12,000 K, 14,000 K and 16,000 K). Left semi-plane – laminar plasma impinging-jets; right semi-plane – turbulent plasma impinging-jets. $L = 10$ mm.

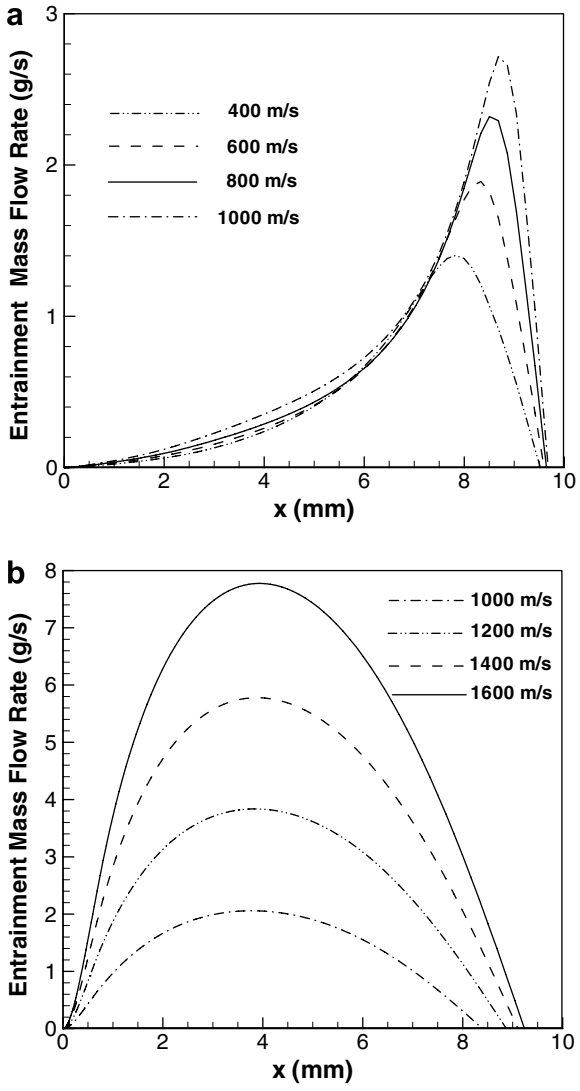

Fig. 7. Variations with the axial distance of the mass flow rate of air entrained into the impinging plasma jets for the cases with a fixed jet-inlet temperature ($T_0 = 14{,}000$ K) but different jet-inlet velocities (U_0): (a) laminar plasma jets, $U_0 = 400$, 600, 800 and 1000 m s^{-1}, (b) turbulent plasma jets, $U_0 = 1000$, 1200, 1400 and 1600 m s^{-1}. $L = 10$ mm.

in Eq. (11) and the plate standoff distance $L = 10$ mm, Fig. 2 compares the computed streamlines in the laminar (upper semi-plane) and turbulent (lower semi-plane) plasma impinging-jets. Corresponding computed isolines of the plasma temperature, axial velocity and argon mass fraction in the impinging plasma jets are compared in Figs. 3–5. It can be seen from the computed streamlines shown in the upper semi-plane of Fig. 2 that the ambient air is first continuously entrained into the laminar plasma impinging-jet, and the forward-flowing main jet changes its flow direction as it approaches to the plate and transforms into an axi-symmetrical radial wall jet, which flows outward along the plate surface into the ambient air. The ambient air is also entrained into the wall jet, and thus the existence of the flat plate significantly enhances the air entrainment rate. There is a distinct difference between the flow pattern in the turbulent plasma impinging-jet shown in the lower semi-plane of Fig. 2 and its laminar counterpart shown in the upper semi-plane of Fig. 2 for the present case with comparatively small plate standoff distance ($L = 10$ mm). Namely, a large axi-symmetrical closed recirculation vortex, which does not occur in the laminar impinging-jet, appears in the turbulent plasma impinging-jet. The reason for such a large closed recirculation vortex to appear in the turbulent impinging-jet is as follows: since turbulent transport mechanism is dominant in the turbulent jet, instead of the molecular transport mechanism in the laminar jet, the ability of the turbulent jet to entrain the surrounding gas is much larger than that of the laminar

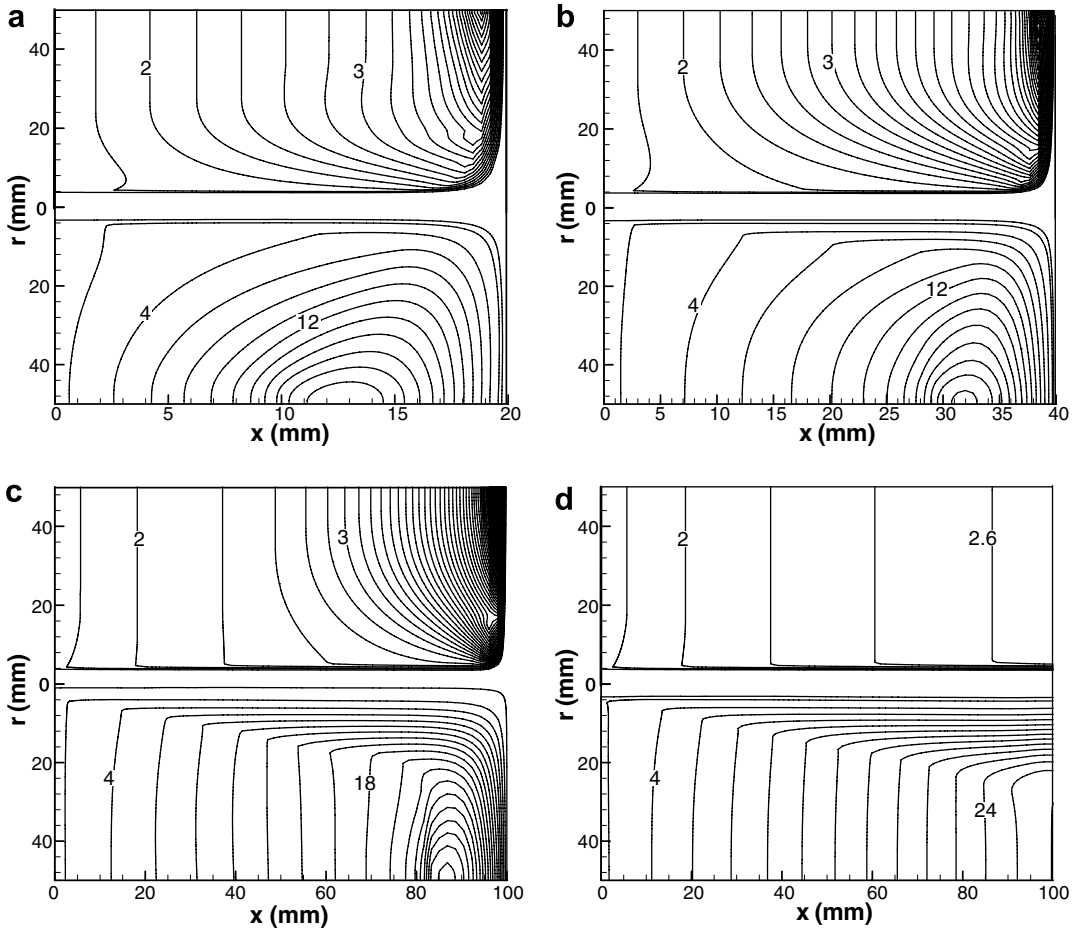

Fig. 8. Comparison of the computed streamlines in the plasma jets. $U_0 = 1000$ m s^{-1} and $T_0 = 14{,}000$ K. The stream function is presented in 10^{-4} kg s^{-1} per radian: (a) $L = 20$ mm, (b) $L = 40$ mm, (c) $L = 100$ mm, (d) $L = 100$ mm, (a)–(c) impinging-jet, (d) free jet. Upper semi-planes – laminar plasma jet, interval – 0.2×10^{-4} kg s^{-1} per radian; lower semi-planes – turbulent plasma jet, interval – 2×10^{-4} kg s^{-1} per radian.

jet [26]. Comparison of the computed streamlines shown in the upper and lower semi-planes of Fig. 2 shows that even at the cross section 2 mm from the jet inlet, the mass flow rate of the ambient air entrained into the turbulent plasma impinging-jet has already been approximately equal to that into the whole laminar plasma impinging-jet for this case with $L = 10$ mm. As a result, there is no enough time for the turbulent plasma impinging-jet to entrain enough gas directly from the ambient air to satisfy its higher entrainment requirement at the jet downstream region. Instead, a part of the argon–air mixture is recirculating to serve as the gas entrained into both the turbulent forward-flowing main jet and the outward-flowing radial wall jet to fulfill their higher entrainment requirement. Due to the existence of such a large closed recirculation vortex in the turbulent plasma impinging-jet, the outermost isolines of the plasma temperature and argon mass fraction are pushed towards the left-hand side, as seen in the lower semi-planes of Figs. 3 and 5, respectively. The outermost isoline of axial velocity shown in the lower semi-plane of Fig. 4 is less influenced since the magnitudes of the reverse flow velocity in the recirculation vortex are much less than 100 m s^{-1}.

Fig. 6 compares the heat flux density distributions on the plate surface for the laminar (left semi-plane) and turbulent (right semi-plane) plasma impinging-jets with fixed plate standoff distance ($L = 10$ mm) and jet-inlet velocity ($U_0 = 1000$ m s^{-1}) but different jet-inlet temperatures ($T_0 = 10{,}000$, 12,000, 14,000 and 16,000 K). For a given combination of jet-inlet temperature and velocity, the calculated heat flux density on the plate surface assumes its maximum value at the jet axis and decreases rapidly in the radial direction. As expected, the maximum heat flux density increases with increasing jet-inlet temperature. It is noted that for the present case with small plate standoff distance ($L = 10$ mm), there is no appreciable difference between the laminar and turbulent plasma impinging-jets in their maximum values and distributions of the calculated heat flux density and even narrower radial profiles are obtained for the turbulent jet case. This prediction is not consistent with usual anticipation (smaller peak values and wider radial profiles for a turbulent jet), and is caused by the presence of the closed recirculation vortex in the turbulent plasma impinging-jet, which compresses the forward-flowing main jet, prevents the expanding of the turbulent impinging-jet and reduces the

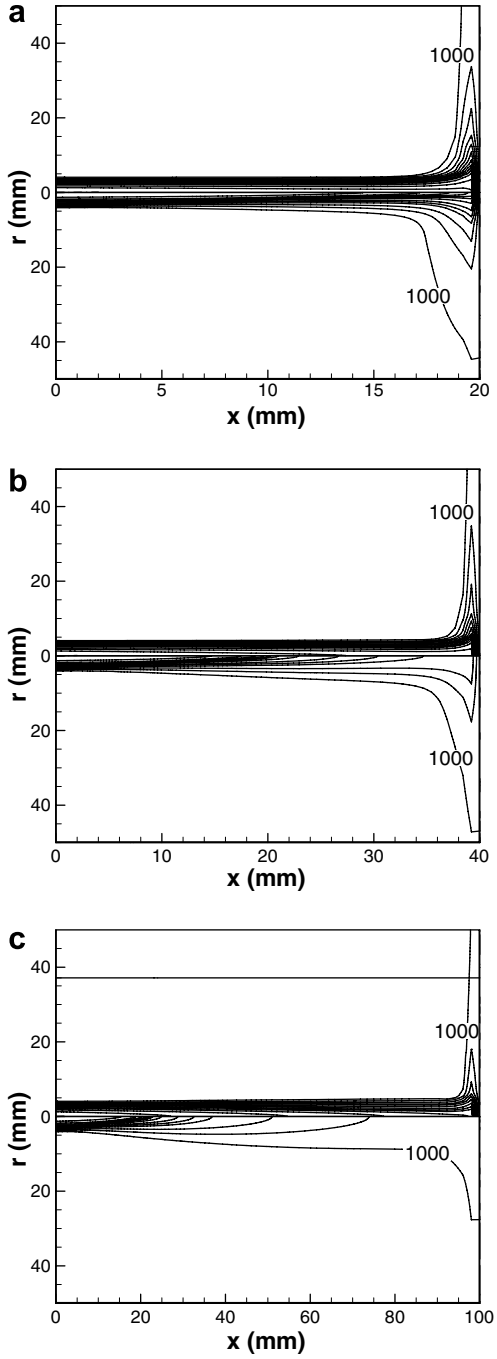

Fig. 9. Comparison of the computed temperature fields in the laminar (upper semi-planes) and turbulent (lower semi-planes) plasma impinging-jets. Outermost isotherm – 1000 K, isotherm interval – 1000 K: (a) $L = 20$ mm, (b) $L = 40$ mm, (c) $L = 100$ mm. $U_0 = 1000\ \mathrm{m\ s^{-1}}$ and $T_0 = 14{,}000$ K.

net air flow rate entrained into the turbulent plasma impinging-jet. For the cases with fixed plate standoff distance ($L = 10$ mm) and jet-inlet temperature but different jet-inlet velocities, computed results show that the maximum heat flux density increase with increasing jet-inlet velocity, as expected.

Similar modeling results are also obtained concerning the pressure and shear stress distributions at the plate surface, i.e. there is no appreciable difference between the laminar and turbulent plasma impinging-jets in their calculated maximum values and distributions of the surface pressure and shear stress for the case with $L = 10$ mm.

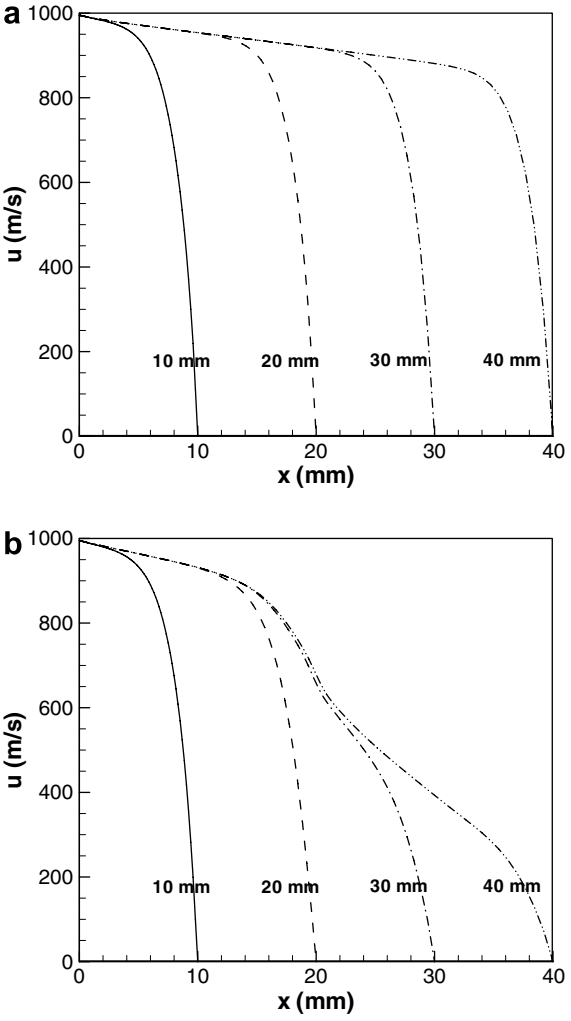

Fig. 10. Variations of the plasma axial velocity along the axis of the impinging plasma jet for different plate locations. $T_0 = 14{,}000$ K and $U_0 = 1000\ \mathrm{m\ s^{-1}}$: (a) laminar jets, (b) turbulent jets. The numerals within the figures denote the plate standoff distances.

The total axial mass flux will unceasingly increase in the axial direction of a freely flowing plasma jet due to the continuous entrainment of surrounding gas into the jet [26]. However, for the impinging plasma jet under study, the total axial mass flux increases at first due to the entrainment of ambient air into the main jet but decreases as the main jet approaches to the flat plate, which forces the jet change its flow direction and out-flow from the computational domain as a radial wall jet. The net axial mass flux of the ambient air entrained into the plasma jet, which is equal to the local axial mass flux minus that at the jet inlet, at the location with an axial distance x from the jet inlet is calculated by

$$F_e = \int_0^R 2\pi\rho u r\,\mathrm{d}r - \left(\int_0^R 2\pi\rho u r\,\mathrm{d}r\right)_{\text{inlet}} \tag{14}$$

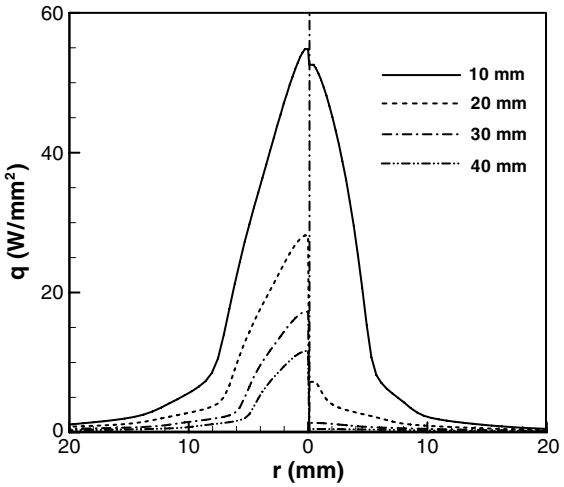

Fig. 11. Comparison of the computed heat flux density distributions on the plate surface for the cases with fixed jet-inlet temperature ($T_0 = 14{,}000$ K) and velocity ($U_0 = 1000$ m s^{-1}) but different plate standoff distances for the laminar (left semi-plane) and turbulent (right semi-plane) plasma impinging-jets.

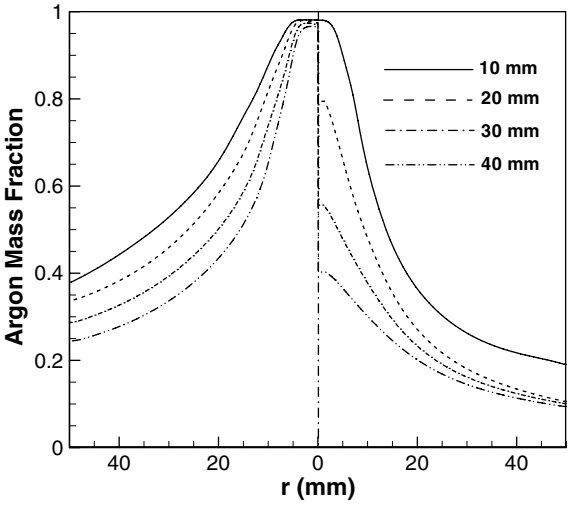

Fig. 12. Comparison of the computed argon mass fraction distributions on the plate surface for the cases with fixed jet-inlet temperature ($T_0 = 14{,}000$ K) and velocity ($U_0 = 1000$ m s^{-1}) but different plate standoff distances for the laminar (left semi-plane) and turbulent (right semi-plane) plasma impinging-jets.

where R is the outer radius of the computational domain, i.e. 50 mm. Fig. 7 compares the computed axial variations of the net axial mass flux in the laminar (a) and turbulent (b) plasma impinging-jets for the cases with fixed plate standoff distance ($L = 10$ mm) and jet-inlet temperature ($T_0 = 14{,}000$ K) but different jet-inlet axial velocities ($U_0 = 400$, 600, 800 and 1000 m s^{-1} for laminar jets, whereas $U_0 = 1000$, 1200, 1400 and 1600 m s^{-1} for turbulent jets). It is seen from Fig. 7(a) that for a given jet-inlet velocity, the net axial mass flux F_e in the laminar plasma impinging-jet at first increases monotonously in the main jet region and then decreases rapidly as the forward-flowing main jet approaches to the plate due to that the gas turns to out-flow as a radial wall jet and leaves from the computational domain. It is noted that the net axial mass flux F_e has dropped to zero at a certain location with distance Δ_L from the plate surface. It means that the mass flow rate out-flowing from the computational domain between the section with the axial location $x = L - \Delta_L$ and the plate surface ($x = L$) is equal to the jet-inlet mass flow rate. With the increase of the jet-inlet velocity, the maximum net axial mass flux F_e increases but the Δ_L decreases (associated with the increase of the velocities in wall jet). On the other hand, Fig. 7(b) shows that for a given jet-inlet velocity, the net axial mass flux F_e in the turbulent plasma impinging-jet assumes its maximum much earlier than the laminar case due to the existence of the large closed recirculation vortex and the net axial mass flux drops to zero at a distance Δ_T from the plate surface. With the increase of the jet-inlet velocity, also the maximum net mass flow rate increases and the Δ_T decreases. However, the maximum net axial mass flux in the turbulent impinging-jet for the case with $U_0 = 1000$ m s^{-1}, $T_0 = 10{,}000$ K and $L = 10$ mm is somewhat less than its counterpart in the laminar impinging-jet. Similar computed results are also obtained for the cases with fixed jet-inlet velocity ($U_0 = 1000$ m s^{-1}) but different jet-inlet temperatures ($T_0 = 10{,}000$, 12,000, 14,000 and 16,000 K). Namely, the maximum net entrained-air flow rates for the turbulent plasma jets appear much earlier than the laminar case (not shown as figures). The maximum net axial mass flux entrained into the laminar or turbulent impinging-jet increases with increasing jet-inlet velocity, as shown in Fig. 7, but decreases with increasing jet-inlet temperature (or decreasing jet-inlet mass flow rate).

Now we turn to study the effect of the plate standoff distance on the flow and heat transfer characteristics of laminar and turbulent plasma impinging-jets. It is expected that with the increase of the plate standoff distance, the closed recirculation vortex appearing in the flow field of the turbulent plasma impinging-jet, as shown in the lower semi-plane of Fig. 2 for $L = 10$ mm, will move downstream, shrink in sizes and then disappear at large L values. The effects of the plate standoff distance on the flow patterns in laminar plasma impinging-jets are shown in the upper semi-planes and corresponding results for the turbulent plasma impinging-jets are shown in the lower semi-planes of Fig. 8 under the same jet-inlet conditions and for larger plate standoff distances ($L \geqslant 2$ mm). It is seen from Fig. 8(a)–(c) that the flow patterns in the laminar plasma impinging-jets for different plate standoff distances (20, 40 and 100 mm) are qualitatively similar, i.e. the ambient air is continuously entrained into the main jet and the forward-flowing main jet changes its flow direction when it approaches to the plate and turns into a radial wall jet out-flowing from the computational domain. It is found that the existence of the flat plate not only forces the forward-flowing main jet change its flow direction but also significantly enhances the mass flow rate of the ambient air entrained into the laminar impinging-jet due to the additional entrainment of the wall jet, as is demonstrated by comparing the computed streamlines shown in the upper

semi-plane of Fig. 8(c) (impinging-jet) with those in Fig. 8(d) (free jet) for $L = 100$ mm. The flow rate of the ambient air entrained into the laminar plasma impinging-jet increases with increasing plate standoff distance L, but is not directly proportional to L. It is also seen from the lower semi-planes of Fig. 8 that when the plate standoff distance is $\geqslant 20$ mm, the flow patterns in the turbulent plasma impinging-jets are also qualitatively similar, i.e. the ambient air is continuously entrained into the main jet and the forward-flowing jet changes its flow direction as it approaches to the plate and turns into a radial wall jet out-flowing from the computational domain. The existence of the flat plate also appreciably enhances the air entrainment into the turbulent plasma impinging-jets, as is demonstrated by comparing the computed streamlines shown in the lower semi-plane of Fig. 8(c) (impinging-jet) with those shown in the lower semi-plane of Fig. 8(d) (free jet) for $L = 100$ mm. The mass flow rates of the ambient air entrained into the turbulent plasma free-jets are much greater than their laminar counterparts, and thus the expanding angles of the turbulent jets are larger than their laminar counterparts [26]. The same conclusion is also qualitatively applicable to the turbulent plasma impinging-jets for the case with the plate standoff distance $\geqslant 20$ mm. However, the case with the plate standoff distance $L = 10$ mm is quite different, where a large closed recirculation vortex appears in the flow field of the turbulent plasma impinging-jet and the net air entrainment rate is reduced, as discussed above associated with Fig. 2.

Fig. 9 compares the computed temperature distributions in laminar (upper semi-planes) and turbulent (lower semi-planes) plasma impinging-jets for the cases with the same jet-inlet temperature ($T_0 = 14{,}000$ K) and velocity ($U_0 = 1000$ m s^{-1}) but different plate standoff distances ($L = 20$, 40 and 100 mm). It is seen that when the plate standoff distance is comparatively large (>20 mm), the plasma temperature at the outer edge of stagnation-point boundary layer on the plane surface for the laminar jet is appreciably higher than that for the turbulent jet due to larger entrained flow rate of the ambient air and thus rapider decaying rate of plasma temperature are involved in the turbulent jet. The presence of the flat plate only affects on the temperature distributions in the near-plate region of the impinging plasma jets, while the temperature distributions in the upstream region of the plasma jets are less influenced and almost identical to corresponding free plasma jets. Similar conclusion is also obtained from comparing the computed axial velocity or argon mass fraction distributions in laminar and turbulent plasma impinging-jets for the cases with the same T_0 and U_0 but different plate standoff distances (not shown here as separate figures). On the other hand, when the plate standoff distance is small (e.g. for $L = 10$ mm), the difference between laminar and turbulent plasma impinging-jets in their high-temperature regions is not appreciable due to the presence of the 'potential core' and the large closed recirculation vortex in the turbulent jet, as discussed above associated with Figs. 3 and 6.

The mentioned impinging-jet behavior is revealed more clearly in Fig. 10. Fig. 10 shows the variations of plasma axial velocity along the axis of the laminar (a) and turbulent (b) plasma impinging-jets for a few different plate standoff distances, respectively. In this figure, the numerals represent the plate standoff distances, i.e. $L = 10$, 20, 30 and 40 mm, respectively. Since the unceasing entrainment of ambient air into the plasma jets, the plasma axial velocity always decreases with increasing axial distance from the jet inlet, and rapider decreases only appear in the region near the plate surface. It means that the presence of plate only affect appreciably the axial velocity distribution in the region near the plate. Corresponding computed results concerning the variations of plasma temperature along the axis of the laminar and turbulent plasma impinging-jets also show that the plasma temperature always decreases with increasing axial distance due to the air entrainment, and rapider decreases only appear in the region near the plate surface (not shown here as separate figures). The plate affecting-zones for the plasma temperature distributions are even narrower than those for the axial velocity distributions along the jet axis.

Figs. 11 and 12 compare the computed heat flux density and argon mass fraction distributions on the plate surface for the laminar (on left semi-planes) and turbulent (on right semi-planes) plasma impinging-jets with the same T_0 and U_0 but different plate standoff distances, respectively. It is seen that the maximum values of heat flux density and argon mass fraction decrease with increasing plate standoff distance, but the decreasing rates of the maximum heat flux density and argon mass fraction for the laminar plasma impinging-jets are much less than their counterparts for the turbulent plasma impinging-jets. The argon mass fractions at the plate center for the laminar plasma jets are appreciably higher than their turbulent counterparts for the cases with larger plate standoff distances.

It is expected that if a larger radial size of the computational domain (e.g. larger than 50 mm) is used, the maximum mass flow rate of ambient air entrained into the impinging plasma jet will increase, mainly due to that more air will be entrained into the wall jet region as the radial size increases. However, such an additional air entrainment of the wall jet with larger radial distance does not affect appreciably the flow, temperature and argon concentration fields as well as the wall heat flux distribution in the central region of the impinging plasma jets, and thus less influences the plasma materials processing.

The LTE assumption has been used in this modeling study. It is anticipated that non-LTE effects may appear near the plate surface or near the outer edge of the plasma jet. Including the non-LTE effects in the modeling will be the subject of subsequent studies.

4. Conclusions

Understanding the different characteristics of laminar and turbulent plasma impinging-jets is important for the applications of the plasma jets in materials processing.

Modeling results concerning the characteristics of laminar and turbulent argon plasma jets impinging normally upon a flat plate in ambient air show that due to the additional entrainment produced by the wall jet flowing along the plate surface, the mass flow rate of the ambient air entrained into the impinging-jet is more than that into corresponding free jet. The plasma parameters (temperature, axial velocity, argon mass fraction, etc.) are affected by the presence of the plate mainly in the near-plate region, and the decaying rates of the plasma parameters in the turbulent impinging-jet are often appreciably larger than their laminar counterparts due to that more air is entrained into the turbulent jet. However, for the case with the short plate standoff distance ($L = 10$ mm) typical for plasma re-melting or cladding hardening of materials surfaces, it is found that there exists a larger closed recirculation vortex in the turbulent impinging-jet. As a result, only a little difference exists between the two types of jets in their maximum values and radial distributions of the heat flux density at the plate surface under the same jet-inlet conditions for this case.

Acknowledgement

This study was supported by the National Natural Science Foundation of China (Nos. 50336010, 10405015, 10575127).

References

[1] E. Pfender, Thermal plasma technology: where do we stand and where are we going? Plasma Chem. Plasma Process. 19 (1) (1999) 1–31.
[2] P. Fauchais, Understanding plasma spraying, J. Phys. D: Appl. Phys. 37 (9) (2004) R86–R108.
[3] N. El-Kaddah, J. McKelliget, J. Szekely, Heat transfer and fluid flow in plasma spraying, Metall. Trans. B 15B (1) (1984) 59–70.
[4] Y.C. Lee, E. Pfender, Particle dynamics and particle heat and mass transfer in thermal plasmas. Part III. Thermal plasma jet reactor and multiparticle injection, Plasma Chem. Plasma Process. 7 (1) (1987) 1–27.
[5] Y.P. Chyou, E. Pfender, Modelling of plasma jets with superimposed vortex flow, Plasma Chem. Plasma Process. 9 (2) (1989) 291–328.
[6] E. Pfender, J. Fincke, E. Spores, Entrainment of cold gas into thermal plasma jets, Plasma Chem. Plasma Process. 11 (4) (1991) 529–543.
[7] J.R. Fincke, C.H. Chang, W.D. Swank, D.C. Haggard, Entrainment and demixing in subsonic thermal plasma jets: comparison of measurements and predictions, Int. J. Heat Mass Transfer 37 (11) (1994) 1673–1682.
[8] A. Vardelle, P. Fauchais, B. Dussoubs, N.J. Themelis, Heat generation and particle injection in a thermal plasma torch, Plasma Chem. Plasma Process. 18 (4) (1998) 551–574.
[9] P. Fauchais, V. Vardelle, Heat, mass and momentum transfer in coating formation by plasma spraying, Int. J. Therm. Sci. 39 (9–11) (2000) 852–870.
[10] R. Bolot, M. Imbert, C. Coddet, On the use of a low Reynolds number extension to the Chen–Kim (k–ε) model to predict thermal exchanges in the case of an impinging plasma jet, Int. J. Heat Mass Transfer 44 (6) (2001) 1095–1106.
[11] H.P. Li, Xi Chen, Three-dimensional modeling of the turbulent plasma jet impinging upon a flat plate and with transverse particle and carrier-gas injection, Plasma Chem. Plasma Process. 22 (1) (2002) 27–58.
[12] D.T. Gawne, T. Zhang, B. Liu, Computational analysis of the influence of a substrate, solid shield and gas shroud on the flow field of a plasma jet, Surf. Coat. Technol. 153 (2–3) (2002) 138–147.
[13] J.R. Fincke, D.M. Crawford, S.C. Snyder, W.D. Swank, D.C. Haggard, R.L. Williamson, Entrainment in high-velocity, high-temperature plasma jets. Part 1: Experimental results, Int. J. Heat and Mass Transfer 46 (22) (2003) 4201–4213.
[14] R.L. Williamson, J.R. Fincke, D.M. Crawford, S.C. Snyder, W.D. Swank, D.C. Haggard, Entrainment in high-velocity, high-temperature plasma jets. Part II: Computational results and comparison to experiment, Int. J. Heat Mass Transfer 46 (22) (2003) 4215–4228.
[15] K. Cheng, Xi Chen, Prediction of the entrainment of ambient air into a turbulent argon plasma jet using a turbulence-enhanced combined-diffusion-coefficient method, Int. J. Heat Mass Transfer 47 (23) (2004) 5139–5148.
[16] A.A. El-Hadj, N. Ait-Messaoudene, Comparison between two turbulence models and analysis of the effect of substrate movement on the flow field of a plasma jet, Plasma Chem. Plasma Process. 25 (6) (2005) 699–722.
[17] V. Kuz'min, O. Solonenko, M. Zhukov, Application of DC plasma torch with a quasilaminar jet outflow for coating treatment, in: Proc. 8th Nat. Thermal Spray Conf., Houston, September 11–15, 1995, pp. 83–89.
[18] K. Osaki, O. Fukumasa, High thermal efficiency-type laminar jet generator for plasma processing, Vacuum 59 (1) (2000) 47–54.
[19] W.X. Pan, W. Hua Zhang, W. Hong Zhang, C.K. Wu, Generation of long, laminar plasma jets at atmospheric pressure and effects of flow turbulence, Plasma Chem. Plasma Process. 21 (1) (2001) 23–35.
[20] W.X. Pan, W.H. Zhang, W. Ma, C.K. Wu, Characteristics of argon laminar DC plasma jet at atmospheric pressure, Plasma Chem. Plasma Process. 22 (2) (2002) 271–283.
[21] W.X. Pan, G. Li, X. Meng, W. Ma, C.K. Wu, Laminar plasma jets: generation, characterization, and applications for materials surface processing, Pure Appl. Chem. 77 (2) (2005) 373–378.
[22] W.X. Pan, X. Meng, Xi Chen, C.K. Wu, Experimental study on the thermal argon plasma generation and jet length change characteristics, Plasma Chem. Plasma Process. 26 (4) (2006) 335–345.
[23] W.X. Pan, W. Ma, C.K. Wu, Surface materials processing with DC laminar plasma jets, in: Y.C. Zhou, Y.X. Gu, Z. Li (Eds.), Mechanics and Material Engineering for Science and Experiments, Science Press, Beijing, 2001, pp. 427–431.
[24] W.X. Pan, X. Meng, G. Li, Q.X. Fei, C.K. Wu, Feasibility of laminar plasma-jet hardening of cast iron surface, Surf. Coat. Technol. 197 (2–3) (2005) 345–350.
[25] W. Ma, Q.X. Fei, W.X. Pan, C.K. Wu, Investigation of laminar plasma cladding processing, Appl. Surf. Sci. 252 (10) (2006) 3541–3546.
[26] K. Cheng, Xi Chen, W.X. Pan, Comparison of laminar and turbulent thermal plasma jet characteristics – a modeling study, Plasma Chem. Plasma Process. 26 (3) (2006) 211–235.
[27] C. Zhao, F. Tian, H.R. Peng, J.Y. Hou, Non-transferred arc plasma cladding of stellite Ni60 alloy on steel, Surf. Coat. Technol. 155 (2–3) (2002) 80–84.
[28] H. Martin, Heat and mass transfer between impinging gas jets and solid surfaces, in: J.P. Hartnett, T.F. Irvine Jr. (Eds.), Advances in Heat Transfer, vol. 13, Academic Press, New York, 1977, pp. 1–60.
[29] K. Jambunathan, E. Lai, M.A. Moss, B.L. Button, A review of heat transfer data for single circular jet impingement, Int. J. Heat Fluid Flow 13 (2) (2002) 106–115.
[30] R. Viskanta, Heat transfer to impinging isothermal gas and flame jets, Exp. Therm. Fluid Sci. 6 (2) (1993) 111–134.
[31] A.B. Murphy, Diffusion in equilibrium mixtures of ionized gases, Phys. Rev. E 48 (5) (1993) 3594–3603.

[32] A.B. Murphy, Transport coefficients of air, argon–air, nitrogen–air, and oxygen–air plasmas, Plasma Chem. Plasma Process. 15 (2) (1995) 279–307.

[33] K. Cheng, Xi Chen, Effects of natural convection on the characteristics of long laminar argon plasma jets issuing upwards or downwards into ambient air—a numerical study, J. Phys. D: Appl. Phys. 37 (17) (2004) 2385–2391.

[34] D.Y. Xu, Xi Chen, W.X. Pan, Effects of natural convection on the characteristics of a long laminar argon plasma jet issuing horizontally into ambient air, Int. J. Heat Mass Transfer 48 (15) (2005) 3253–3255.

[35] S.V. Patankar, Numerical Heat Transfer and Fluid Flow, McGraw-Hill, New York, 1980.